

Perturbative Theory of Grazing-Incidence Diffuse Nuclear Resonant Scattering of Synchrotron Radiation

L. Deák,^{1,*} L. Bottyán,¹ D.L. Nagy,¹ H. Spiering,² Yu.N. Khaidukov,³ and Y. Yoda⁴

¹*KFKI Research Institute for Particle and Nuclear Physics,
P.O.B. 49, H-1525 Budapest, Hungary*

²*Institut für Anorganische und Analytische Chemie,
Johannes Gutenberg Universität Mainz,
Staudinger Weg 9, D-55099 Mainz, Germany*

³*Frank Laboratory of Neutron Physics,
Joint Institute for Nuclear Research,
141980, Dubna, Moscow Region, Russia*

⁴*SPring-8 JASRI, 1-1-1 Kouto Mikazuki-cho Sayo-gun Hyogo 679-5198, Japan*

(Dated: August 7, 2021)

Abstract

Theoretical description of off-specular grazing-incidence nuclear resonant scattering of synchrotron radiation (Synchrotron Mössbauer Reflectometry, SMR) is presented. The recently developed SMR, similarly to polarized neutron reflectometry (PNR), is an analytical tool for the determination of isotopic and magnetic structure of thin films and multilayers. It combines the sensitivity of Mössbauer spectroscopy to hyperfine interactions and the depth selectivity of x-ray reflectometry. Specular reflection provides information on the depth profile, while off-specular scattering on the lateral structure of scattering layers. Off-specular SMR and PNR intensity formulae of a rather general multilayer with different domains, based on a Distorted Incident-Wave Approximation (DIWA) are presented. The Distorted-Wave Born Approximation (DWBA) results are given in an Appendix. Physical and numerical implications, why using DIWA, are explained. The temporal character of SMR imposes specific differences between SMR and PNR. In order to reveal the limits of DIWA and to compare the two analytical methods, two-dimensional diffuse SMR and PNR maps of an antiferromagnetic multilayer are calculated and critically compared. Experimental $\omega - 2\theta$ SMR map of a periodic $[\text{Fe}/\text{Cr}]_{20}$ multilayer is presented and compared with simulations by the present theory.

PACS numbers: PACS: 42.25-p, 61.10.Kw, 61.12.Ha, 75.25.+z

Keywords: Reflectometry, grazing incidence, diffuse scattering, distorted wave approximation, nuclear resonance scattering, neutron scattering, multilayers

I. INTRODUCTION

Grazing-incidence reflection from flat surfaces of x-rays,^{1,2,3,4} neutrons^{2,3,4,5,6,7} and of soft x-rays near the absorption edges^{4,8,9} (x-ray, neutron and resonant magnetic x-ray reflectometry, respectively) have been widely used to investigate the chemical, isotopic and magnetic structure of thin films and multilayers (ML).^{10,11,12} Making use of the sensitivity of nuclear resonant scattering (NRS) of synchrotron radiation (SR) to hyperfine interactions, another analytical method has been developed that combines the sensitivity of Mössbauer spectroscopy to hyperfine interactions with the depth information yielded by reflectometry. NRS of SR is performed in the time domain. All nuclear resonances (of typically a few neV linewidth) are excited simultaneously by a SR pulse of a few meV bandwidth. Time-differential NRS of SR contains the hyperfine interaction information in the quantum-beat pattern of the time response that follows the excitation of the system by the synchrotron pulse. Counting, however, all delayed (i.e., nuclear resonant scattered) photons as a function of the grazing angle of incidence is a special kind of x-ray reflectometry that we shall call henceforth Synchrotron Mössbauer Reflectometry (SMR).^{13,14} This method is similar to polarized neutron reflectometry (PNR) and yields integral hyperfine depth profile and superstructure information. Specular SMR has by now become an established technique.^{14,15,16,17}

The specularly reflected radiation from a stratified system is insensitive to the lateral structure; it depends solely on the lateral averages of the material parameters² for the coherence volume.¹⁸ If one uses radiation of infinite coherence length, the contrast of laterally compensated domains (e.g. the magnetic contrast of an antiferromagnetic ML stack) would be absent from the specular reflectivity. However, this is not the case, since the coherent averaging has to be performed for the finite coherence volume¹⁸ of the radiation determined by the experimental setup and such contributions are to be added incoherently.¹⁹

For studying lateral inhomogeneities, such as structural roughness, magnetic domains, etc., diffuse scattering, i.e. off-specular reflectometry is used. ('Diffuse' and 'off-specular' will be used as synonyms throughout this present paper.) Off-specular non-polarized¹² and polarized neutron reflectometry,^{5,11} soft-x-ray resonant magnetic diffuse scattering¹⁰ and, recently, off-specular SMR²⁰ have been used to estimate the domain-size distribution and to follow domain transformations in antiferromagnetically (AF)-coupled magnetic MLs.

The optical theory of *specular* SMR has been published using several, somewhat different

approaches,^{17,21,22,23,24,25,26,27,28,29} however, to our knowledge, the present attempt is the first one to describe nuclear resonant diffuse scattering. Distorted-Wave Born Approximation³⁰ (DWBA) was used earlier by several authors^{19,31,32,33} to describe off-specular scattering of *neutrons* by a rough surface. DWBA perturbatively determines the (off-specular) field^{3,34,35,36} around the specular field, the latter being easily calculated, even for general stratified media, by suitable matrix methods.^{17,19,21,31,37,38,39}

The choice of DWBA to elaborate *off-specular* SMR data seems, therefore, obvious. However, unlike PNR, in the SMR case the scattering potential is strongly energy dependent. Moreover, SMR is detected in the time domain. Therefore the existing theory can not be directly applied. Since the 2D diffuse maps have to be calculated for typically a thousand time- (or energy) channels, therefore, in practice, the anyway long calculation time of the diffuse maps by an orthodox DWBA would multiply by a thousand and become intolerable long for SMR.

The aim of the present paper is to present an alternative general evaluation algorithm for off-specular SMR. A distorted-wave approximation will be used, which is — except for *exit* angles in the total reflection region — accurate enough and, at the same time, it is capable of handling the immense computational problem in a reasonable period of time. For reasons explained in Sec. III, we shall call this approximation 'Distorted Incident-Wave Approximation' (DIWA).

Starting from Lax' general theory² and from the common optical formalism of polarized neutron and Mössbauer reflectometry,²¹ an expression will be deduced for diffuse scattering of electromagnetic and/or quantum mechanical particle waves on laterally inhomogeneous stratified media. From the point of view of specular reflection, the set of discrete atomic scattering centers will be replaced by a homogeneous index of refraction n and the scattering problem will be traced back to solving the wave equation (far from Bragg reflections).² In the rest of the paper the grazing-incidence limit is studied, for which the index of refraction approximation is justified.^{17,24,27,28,29}

The material of the paper is organized as follows. In Sec. II, we present a distorted-wave approximation without treating the energy dependence of the problem. The presented method is a generalization of Vineyard's approximation³⁴ for the case of MLs having domain-like inhomogeneities with absorptive anisotropic index of refractions (scattering potentials). In Sec. III time-differential and time-integral diffuse intensities are derived for quite general

inter- and intra-layer correlations using a domain correlation matrix. The coherent-field solution and the cumulative transmissivity for an arbitrary depth is calculated in Appendices A and B, respectively. The DWBA formulae for the delayed reflectivity are given in Appendix C. In Sec. IV we provide numerical simulations in the DIWA approach for both PNR and SMR. Specular and diffuse PNR and SMR scans and maps are compared and the special features of the methods are discussed. In Sec. IV D the developed DIWA SMR theory is applied to extract the average antiferromagnetic domain size from experimental SMR $\omega - 2\theta$ maps of an [Fe/Cr] epitaxial ML.

II. OFF-SPECULAR SCATTERING

The model systems of the present paper are MLs and thin films, having lateral inhomogeneities on the mesoscopic scale. Unlike the case of surface roughness, these inhomogeneities (domains) will be assumed to be much larger than the atomic distances. In each homogeneous part around position \mathbf{r} an index of refraction $n(\mathbf{r})$ is defined. Since the elements of n for both slow neutrons and X-rays differ only slightly (typically $10^{-2} - 10^{-5}$) from that of the 2×2 unit matrix I , the small parameter, namely the generalized susceptibility, $\chi(\mathbf{r}) = 2[n(\mathbf{r}) - I]$ can be conveniently defined.^{21,27,40}

Using the index-of-refraction approximation, in each homogeneous part of the system, the solution of the homogeneous wave equation

$$[\Delta + k^2 I] \Psi(\mathbf{r}) = -k^2 \chi(\mathbf{r}) \Psi(\mathbf{r}) \quad (2.1)$$

yields $\Psi(\mathbf{r})$, representing the two components of the photon field or the neutron quantum mechanical spinor state at position \mathbf{r} , with k being the wave number in vacuum. χ is simply related to the coherent forward-scattering amplitude f by $\chi = \frac{4\pi N}{k^2} f$ where N is the number of scattering centers per unit volume.^{21,27} For photons $f = f_e + f_n$ is the sum of the electronic and nuclear scattering amplitudes.⁴¹ For neutrons $f = f_{\text{nuc}} + f_{\text{magn}}$ is the sum of the nuclear and magnetic scattering lengths. In Eq. (2.1) $k^2 \chi$ plays the role of the optical scattering potential (scattering-length density in the neutron literature). For photons χ is the susceptibility and, for sake of simplicity, throughout the paper we shall use this term in its general sense.

Describing the system as a stack of (possibly laterally inhomogeneous) layers, we compose

the susceptibility by

$$\chi(\mathbf{r}) = \sum_{l=1}^S \chi_l(\mathbf{r}_{\parallel}), \quad (2.2)$$

as the sum of the susceptibility functions of the individual layers l ($l = 1..S$, the last layer S being the substrate) depending solely on the in-plane coordinate \mathbf{r}_{\parallel} .

If the homogeneous parts of the system are large compared to the wavelength we may assume that the exact solution $\Psi(\mathbf{r})$ is close to the solution $\Psi_{\text{coh}}(\mathbf{r})$ of the coherent (specular) field equation²

$$[\Delta + k^2 I] \Psi_{\text{coh}}(\mathbf{r}) = -k^2 \sum_{l=1}^S \bar{\chi}_l \Psi_{\text{coh}}(\mathbf{r}), \quad (2.3)$$

which is obtained from Eq. (2.1) by replacing the susceptibilities $\chi_l(\mathbf{r}_{\parallel})$ by the average susceptibility $\bar{\chi}_l$ of each layer l . In order to deduce a perturbative equation, the sum $-k^2 \sum \bar{\chi}_l \Psi(\mathbf{r})$ is added and subtracted on the right-hand side of Eq. (2.1)

$$[\Delta + k^2 I] \Psi(\mathbf{r}) = -k^2 \sum_{l=1}^S \bar{\chi}_l \Psi(\mathbf{r}) - k^2 \sum_{l=1}^S [\chi_l(\mathbf{r}_{\parallel}) - \bar{\chi}_l] \Psi(\mathbf{r}). \quad (2.4)$$

For homogeneous layers $\chi_l(\mathbf{r}_{\parallel}) = \bar{\chi}_l$, *i.e.*, the second sum vanishes on the right, so that Eq. (2.4) reduces to Eq. (2.3), the basic equation of specular reflectometry.^{21,27,33,49}

The general solutions of Eq. (2.4) are searched for in a form

$$\Psi(\mathbf{r}) = \Psi_{\text{coh}}(\mathbf{r}) + \Psi_{\text{off}}(\mathbf{r}) \quad (2.5)$$

where $\Psi_{\text{coh}}(\mathbf{r})$ is the coherent field, which vanishes in any non-specular direction, and $\Psi_{\text{off}}(\mathbf{r})$ is the off-specular field. Substituting Eq. (2.5) into Eq. (2.4) and taking into account Eq. (2.3) we obtain

$$[\Delta + k^2 I] \Psi_{\text{off}}(\mathbf{r}) = -k^2 \sum_{l=1}^S [\chi_l(\mathbf{r}_{\parallel}) - \bar{\chi}_l] \Psi_{\text{coh}}(\mathbf{r}) - k^2 \sum_{l=1}^S \chi_l(\mathbf{r}_{\parallel}) \Psi_{\text{off}}(\mathbf{r}). \quad (2.6)$$

The coherent field $\Psi_{\text{coh}}(\mathbf{r})$, solution of Eq. (2.3), is obtained by the optical method²¹ as

$$\Psi_{\text{coh}}(\mathbf{k}, \mathbf{r}) = T(k_{\perp}, r_{\perp}) \Psi^{\text{in}} \exp(i\mathbf{k}_{\parallel} \mathbf{r}_{\parallel}) \quad (2.7)$$

(see Appendix A) where \perp and \parallel denote the plane-perpendicular and in-plane components of the respective vectors and Ψ^{in} is the amplitude of the incident plane wave of wave vector

$\mathbf{k} = (k_{\perp}, \mathbf{k}_{\parallel})$. Here we introduced the 'cumulative transmittance' of the reflecting film from surface to a depth r_{\perp} by:

$$T(k_{\perp}, r_{\perp}) = L^{[21]}(k_{\perp}, r_{\perp}) [I - R_{\text{sp}}(k_{\perp})] + L^{[22]}(k_{\perp}, r_{\perp}) [I + R_{\text{sp}}(k_{\perp})]. \quad (2.8)$$

$R_{\text{sp}}(k_{\perp})$ is the 2×2 specular reflectivity matrix of the system²¹, $L^{[21]}(k_{\perp}, r_{\perp})$ and $L^{[22]}(k_{\perp}, r_{\perp})$ are the respective 2×2 submatrices of the 4×4 characteristic matrix,^{21,27} L at depth r_{\perp} for an incoming plane wave defined by \mathbf{k} .

The physical interpretation of the inhomogeneous wave equation (2.6) is seen from its right-hand side where the first term gives the source of the off-specular radiation and the second term describes the off-specular field scattered by the entire ML. The off-specular field arises from the coherent field at the lateral inhomogeneities, *i.e.* from the regions where the susceptibility χ differs from its average value $\bar{\chi}$. Eq. (2.6) can be solved iteratively to the prescribed accuracy.

As a first approximation, the second term of the right-hand side of Eq. (2.6) is neglected so that the solution can be obtained using the Green-function technique,

$$\Psi_{\text{off}}(\mathbf{k}, \mathbf{r}) = \frac{k^2}{4\pi} \sum_l \int d^3\mathbf{r}' \frac{\exp(i\mathbf{k}R)}{R} [\chi_l(\mathbf{r}'_{\parallel}) - \bar{\chi}_l] \Psi_{\text{coh}}(\mathbf{k}, \mathbf{r}'), \quad (2.9)$$

where $R = |\mathbf{r} - \mathbf{r}'|$. The approximation requires $\|\Psi_{\text{coh}}(\mathbf{r})\| \gg \|\Psi_{\text{off}}(\mathbf{r})\|$, which condition is fulfilled for magnetic MLs of large enough homogeneous domain size in the vicinity of the specular direction^{20,32} so that the exact solution $\Psi(\mathbf{r})$ is close to the coherent field $\Psi_{\text{coh}}(\mathbf{r})$. When neglecting the second term in Eq. (2.6) the scattering of the off-specular field is neglected. Therefore the present distorted-wave approximation breaks down for *exit angles* near the critical angle of total reflection.

Far from the scatterer, the Fraunhofer approximation

$$\frac{\exp(i\mathbf{k}R)}{R} \approx \frac{\exp(i\mathbf{k}r)}{r} \exp(-i\mathbf{k}'\mathbf{r}') \quad (2.10)$$

is applied with \mathbf{k}' being the wave number vector of the emerging plane wave, with which the final expression for the off-specular field is

$$\Psi_{\text{off}}\left(\mathbf{k}, \mathbf{r} = \frac{\mathbf{k}'}{k}r\right) = \sqrt{\frac{\pi}{2}} \frac{k^2}{r} \exp(i\mathbf{k}r) \sum_l S_l(\mathbf{K}_{\parallel}) T_l(k_{\perp}, k'_{\perp}) \Psi^{\text{in}}, \quad (2.11)$$

with \mathbf{K}_{\parallel} being the in-plane component of the momentum transfer vector $\mathbf{K} = \mathbf{k}' - \mathbf{k}$, and

$$T_l(k_{\perp}, k'_{\perp}) = \frac{1}{\sqrt{2\pi}} \int_{Z_l} dr_{\perp} \exp(-ik'_{\perp}r_{\perp}) T(k_{\perp}, r_{\perp}) \quad (2.12)$$

is the Fourier integral over the one-dimensional interval Z_l of layer l . The expression

$$S_l(\mathbf{K}_{\parallel}) = \frac{1}{2\pi} \int d^2\mathbf{r}_{\parallel} \exp(-i\mathbf{K}_{\parallel} \mathbf{r}_{\parallel}) [\chi_l(\mathbf{r}_{\parallel}) - \bar{\chi}_l] \quad (2.13)$$

is the two-dimensional Fourier transform of $\chi_l(\mathbf{r}_{\parallel}) - \bar{\chi}_l$. $T_l(k_{\perp}, k'_{\perp})$ that can be analytically calculated (See Appendix B).

The off-specular scattered intensity $I_{\text{off}} = (\Psi_{\text{off}}, \Psi_{\text{off}})$ is

$$I_{\text{off}} = \frac{\pi k^4}{2r^2} \sum_{ll'} \left(\Psi^{\text{in}}, T_l^{\dagger}(k_{\perp}, k'_{\perp}) S_l^{\dagger}(\mathbf{K}_{\parallel}) S_{l'}(\mathbf{K}_{\parallel}) T_{l'}(k_{\perp}, k'_{\perp}) \Psi^{\text{in}} \right), \quad (2.14)$$

which, for arbitrary incident polarization, can be rewritten as

$$I_{\text{off}} = \frac{\pi k^4}{2r^2} \sum_{ll'} \text{Tr} \left[T_l^{\dagger}(k_{\perp}, k'_{\perp}) S_l^{\dagger}(\mathbf{K}_{\parallel}) S_{l'}(\mathbf{K}_{\parallel}) T_{l'}(k_{\perp}, k'_{\perp}) \rho \right], \quad (2.15)$$

where ρ is the polarization density matrix of the incident radiation.⁴² From the convolution theorem, it follows that the Fourier transform $\mathfrak{C}_{ll'}(\mathbf{R}_{\parallel})$ of

$$C_{ll'}(\mathbf{K}_{\parallel}) = (2\pi) S_l^{\dagger}(\mathbf{K}_{\parallel}) S_{l'}(\mathbf{K}_{\parallel}) \quad (2.16)$$

is the cross-correlation function of the susceptibilities between layers l and l'

$$\mathfrak{C}_{ll'}(\mathbf{R}_{\parallel}) = \int d^2\mathbf{r}_{\parallel} [\chi_l(\mathbf{R}_{\parallel} + \mathbf{r}_{\parallel}) - \bar{\chi}_l]^{\dagger} [\chi_{l'}(\mathbf{r}_{\parallel}) - \bar{\chi}_{l'}]. \quad (2.17)$$

The final result then becomes

$$I_{\text{off}} = \frac{k^4}{4r^2} \sum_{ll'} \text{Tr} \left[T_l^{\dagger}(k_{\perp}, k'_{\perp}) C_{ll'}(\mathbf{K}_{\parallel}) T_{l'}(k_{\perp}, k'_{\perp}) \rho \right], \quad (2.18)$$

a convenient expression for randomly distributed lateral inhomogeneities. We note that the off-specular intensity $I_{\text{off}} = I_{\text{off}}(\mathbf{K}_{\parallel}, k_{\perp}, k'_{\perp})$ is a function of \mathbf{K}_{\parallel} , k_{\perp} and k'_{\perp} , a notation dropped in the calculations. The corresponding values of \mathbf{K}_{\parallel} , k_{\perp} and k'_{\perp} can be given for the chosen experimental geometry. The diffuse intensity expression in Eq. (2.18) differs from that of DWBA,³⁰ an issue to be discussed in Sec. III and in Appendix C.

A possible experimental realization of the off-specular reflectometry is the so-called 'ω-scan' geometry where the detector position is set to 2θ and the sample orientation ω on the goniometer is varied with the sample normal remaining in the scattering plane. For ω-scans, the in-plane components of the momentum transfer vector K_{\parallel} and the plane-perpendicular

component of the wave vector of the emerging wave k'_\perp can be expressed by the grazing angle θ and by ω :

$$K_\parallel = 2k \sin \theta \sin (\omega - \theta), \quad (2.19)$$

$$k_\perp = k \sin \omega, \quad (2.20)$$

$$k'_\perp = -k \sin (2\theta - \omega). \quad (2.21)$$

One may observe that K_\parallel vanishes at the specular condition $\omega = \theta$. A two-dimensional representation of the full diffuse scatter is the ' $\omega - 2\theta$ '-map. A further, widely used, arrangement is the so-called 'detector scan' geometry in which the angle of incidence θ_{in} is fixed and the scattered intensity is recorded as a function of the exit angle θ_{out} . In case of a detector scan, Eqs. (2.19) and (2.24) read

$$K_\parallel = k (\cos \theta_{\text{out}} - \cos \theta_{\text{in}}), \quad (2.22)$$

$$k_\perp = k \sin \theta_{\text{in}}, \quad (2.23)$$

$$k'_\perp = -k \sin \theta_{\text{out}}, \quad (2.24)$$

with the specular condition being $\theta_{\text{out}} = \theta_{\text{in}}$. An alternative representation of the full diffuse scatter is the ' $\theta_{\text{in}} - \theta_{\text{out}}$ ' map.

III. OFF-SPECULAR SMR

A. Time-differential scattered intensity

Eq. (2.18) for the off-specular intensity is equally valid for neutron and x-ray scattering where the time of the scattering process is negligible. However, in case of nuclear resonant scattering we detect the time response

$$\Psi_{\text{off}}(\mathbf{r}, t) = \frac{1}{\hbar\sqrt{2\pi}} \int_{-\infty}^{\infty} dE \Psi_{\text{off}}(\mathbf{r}, E) \exp(-iEt/\hbar) \quad (3.1)$$

after the synchrotron pulse,⁴³ which is the Fourier transform of the energy-dependent off-specular field. Close to a Mössbauer resonance, both the susceptibilities $\chi_l(\mathbf{r}'_\parallel, E) - \overline{\chi}_l(E)$ and the coherent field $\Psi_{\text{coh}}(\mathbf{r}', E)$ are strongly energy-dependent.⁴³ Therefore, through Eqs. (2.8), (2.12) and (2.13), the $S_l(\mathbf{K}_\parallel, E)$ and the $T_l(k_\perp, k'_\perp, E)$ quantities carry an energy

dependence, too. Consequently, Eq. (2.18) can no longer be applied to calculate the off-specular intensity.

A possible workaround of this problem is to define a distribution function $\Omega_l^\mu(\mathbf{r}_\parallel)$ of homogeneous regions of type $\mu = 1, \dots, M$ of layer l . This function $\Omega_l^\mu(\mathbf{r}_\parallel)$ characterizes the homogeneous regions of layer l of an energy-dependent susceptibility $\chi^\mu(E)$. Over the region of type μ in layer l the distribution function $\Omega_l^\mu(\mathbf{r}_\parallel) = 1$ otherwise $\Omega_l^\mu(\mathbf{r}_\parallel) = 0$. Any point \mathbf{r}_\parallel along the surface of layer l is related to one domain type, therefore

$$\sum_{\mu} \Omega_l^\mu(\mathbf{r}_\parallel) = 1. \quad (3.2)$$

The total inhomogeneous susceptibility is the sum

$$\chi(\mathbf{r}, E) = \sum_{\mu=1}^M \sum_{l=1}^S \Omega_l^\mu(\mathbf{r}_\parallel) \chi^\mu(E) \quad (3.3)$$

where the space- and energy-dependent terms in $\chi(\mathbf{r}, E)$ have been separated. The average susceptibility within layer l is

$$\bar{\chi}_l(E) = \sum_{\mu=1}^M \eta_l^\mu \chi^\mu(E) \quad (3.4)$$

where the fractional domain area is

$$\eta_l^\mu = A_l^\mu / A \quad (3.5)$$

i.e., the ratio of $A_l^\mu = \int d^2\mathbf{r}_\parallel \Omega_l^\mu(\mathbf{r}_\parallel)$, the total area of the homogeneous part of type μ within layer l , and A , the area of the ML. Since the domains fully cover the layers, the condition

$$\sum_{\mu} \eta_l^\mu = 1 \quad (3.6)$$

is fulfilled. Using (3.3) and (3.4), Eq. (2.13) becomes

$$S_l(\mathbf{K}_\parallel, E) = \sum_{\mu=1}^M W_l^\mu(\mathbf{K}_\parallel) \chi^\mu(E) \quad (3.7)$$

with

$$W_l^\mu(\mathbf{K}_\parallel) = \frac{1}{2\pi} \int d^2\mathbf{r}_\parallel \exp(-i\mathbf{K}_\parallel \mathbf{r}_\parallel) [\Omega_l^\mu(\mathbf{r}_\parallel) - \eta_l^\mu] \quad (3.8)$$

and, finally, the energy-dependent off-specular field in the Fraunhofer approximation is

$$\Psi_{\text{off}}(\mathbf{r}, E) = \sqrt{\frac{\pi}{2}} \frac{k^2}{r} \exp(ikr) \sum_{l,\mu} W_l^\mu(\mathbf{K}_\parallel) \chi^\mu(E) T_l(E) \Psi^{\text{in}} \quad (3.9)$$

while the off-specular intensity is

$$I_{\text{off}}(E) = \frac{k^4}{4r^2} \sum_{l'l''} C_{ll''}^{\mu\mu'}(\mathbf{K}_{\parallel}) \text{Tr} \left[\Gamma_l^{\mu}(E)^{\dagger} \Gamma_{l''}^{\mu'}(E) \rho \right]. \quad (3.10)$$

The matrices for the homogeneous region μ, l

$$\Gamma_l^{\mu}(E) = \chi^{\mu}(E) T_l(E) \quad (3.11)$$

are the products of the homogeneous solution $T_l(E)$ and the susceptibility $\chi^{\mu}(E)$ of that region. For the sake of brevity, henceforth the dependence of T_l and Γ_l^{μ} on both k_{\perp} and k'_{\perp} will not be explicitly written.

As we already indicated in the previous section, Eq. (2.18) and, consequently, Eq. (3.10) differ from the usual expression of diffuse intensity of DWBA as published earlier in the literature^{19,30,31,32,33} in such a way, that the "distortions" are only considered on the incident path before scattering, the exit path is left undistorted. The DWBA expression is given and discussed in Appendix C. Physically speaking, the difference between the two approximations is that DIWA only takes distortions into account on the incident wave, while DWBA on both incident and emerging waves. Therefore a DIWA calculation is considerable faster but it is not expected to be invariant with respect to exchanging the source and detector (a condition widely called 'reciprocity'^{44,45,46}). Should, nevertheless, reciprocity be physically justified under some conditions, we may take advantage of calculating only half of the ' $\theta_{\text{in}} - \theta_{\text{out}}$ ' and the ' $\omega - 2\theta$ ' maps along with mirroring one side of the $\theta_{\text{in}} = \theta_{\text{out}}$ line and the $\omega = \theta$ lines onto the other, respectively. We shall see that the DIWA calculation is quite accurate at one side of these lines, a fact finally resulting both in saving another 50 % of the computation time and in a high accuracy of the calculation of the full diffuse scatter.

The geometrical (or 'domain') correlation function $C_{ll''}^{\mu\mu'}$ between layers l and l'' and homogeneous parts μ and μ' of the layers with definition

$$C_{ll''}^{\mu\mu'}(\mathbf{K}_{\parallel}) = (2\pi) W_l^{\mu}(\mathbf{K}_{\parallel})^* W_{l''}^{\mu'}(\mathbf{K}_{\parallel}) \quad (3.12)$$

may describe quite general structural and magnetic intra- and interlayer correlations like correlated layer growth, or magnetic-magnetic correlation (e.g. antiferromagnetic multilayer domains) and even magnetic-structural correlations. Similarly to Eq. (2.17), the direct space correlation function can be written as

$$\mathfrak{C}_{ll''}^{\mu\mu'}(\mathbf{R}_{\parallel}) = \frac{1}{A} \int d^2\mathbf{r}_{\parallel} \left[\Omega_l^{\mu}(\mathbf{R}_{\parallel} + \mathbf{r}_{\parallel}) - \eta_l^{\mu} \right] \left[\Omega_{l''}^{\mu'}(\mathbf{r}_{\parallel}) - \eta_{l''}^{\mu'} \right]. \quad (3.13)$$

Notice that both the correlation function and its Fourier transform are symmetric with respect to the simultaneous exchange of the domain and layer indices:

$$\mathfrak{C}_{ll'}^{\mu\mu'}(\mathbf{R}_{\parallel}) = \mathfrak{C}_{l'l}^{\mu'\mu}(\mathbf{R}_{\parallel}). \quad (3.14)$$

An important consequence of Eqs. (3.2) and (3.6) is

$$\sum_{\mu'} \mathfrak{C}_{ll'}^{\mu\mu'}(\mathbf{R}_{\parallel}) = \sum_{\mu} \mathfrak{C}_{ll'}^{\mu\mu'}(\mathbf{R}_{\parallel}) = 0. \quad (3.15)$$

Using Eq. (3.13) the correlation function at $\mathbf{R}_{\parallel} = 0$ reads

$$\mathfrak{C}_{ll'}^{\mu\mu'}(0) = \eta_{ll'}^{\mu\mu'} - \eta_l^{\mu} \eta_{l'}^{\mu'} \quad (3.16)$$

where

$$\eta_{ll'}^{\mu\mu'} = \frac{1}{A} \int d^2\mathbf{r}_{\parallel} \Omega_l^{\mu}(\mathbf{r}_{\parallel}) \Omega_{l'}^{\mu'}(\mathbf{r}_{\parallel}) \quad (3.17)$$

is the fractional overlap of homogeneous parts of types μ and μ' in layers l and l' , respectively.

In Eq. (3.10) the geometrical correlation is separated from the energy-dependence and, therefore, it can be applied for time and energy domain experiments alike. The Fourier transformation can be performed so that, using Eqs. (3.1) and (3.10), the time-dependent intensity becomes

$$I_{\text{off}}(t) = \frac{k^4}{4r^2} \sum_{l'l'\mu\mu'} C_{ll'}^{\mu\mu'}(\mathbf{K}_{\parallel}) \text{Tr} \left[G_l^{\mu}(t)^{\dagger} G_{l'}^{\mu'}(t) \rho \right] \quad (3.18)$$

where

$$G_l^{\mu}(t) = \frac{1}{\hbar\sqrt{2\pi}} \int_{-\infty}^{\infty} dE \Gamma_l^{\mu}(E) \exp(-iEt/\hbar). \quad (3.19)$$

B. Time-integral scattered intensity

The time-integrated intensity is $I_{\text{off}}^{\text{int}} = \int_{t_1}^{t_2} dt I_{\text{off}}(t)$ where t_1 and t_2 define the starting and finishing time of the time window of the counting after the synchrotron pulse. Applying Eqs. (3.18) and (3.19)

$$I_{\text{off}}^{\text{int}} = \frac{k^4}{4\hbar r^2} \sum_{m=-\infty}^{\infty} s_m \int_{-\infty}^{\infty} dE \sum_{l'l'\mu\mu'} C_{ll'}^{\mu\mu'}(\mathbf{K}_{\parallel}) \text{Tr} \left[\Gamma_l^{\mu}(E + m\varepsilon)^{\dagger} \Gamma_{l'}^{\mu'}(E) \rho \right] \quad (3.20)$$

where $\varepsilon = \frac{\hbar}{t_{\text{bunch}}}$ with t_{bunch} being the time interval between the synchrotron bunches, \hbar is the Planck constant, s_m is the m^{th} discrete Fourier component of the periodical time window function $S(t) = \sum_{m=-\infty}^{\infty} s_m \exp\left(i\frac{2m\pi}{t_{\text{bunch}}}t\right)$ of the experiment defined by $S(t) = 1$ for $t_1 < t < t_2$, otherwise $S(t) = 0$ after each synchrotron bunch.

IV. MODEL CALCULATIONS AND COMPARISON WITH EXPERIMENT

Applying the above theory, off-specular time-integrated SMR curves and maps were calculated and, on one hand, compared with PNR curves and maps simulated with the same DIWA theory and, on the other hand, compared with experimental off-specular SMR data. In order to treat realistic problems, at this point further specification of the studied system and the experimental conditions will be undertaken — without restricting the generality of the discussion. The actual calculations were performed for the $\text{MgO}/[{}^{57}\text{Fe}(2.62\text{ nm})/\text{Cr}(1.28\text{ nm})]_{20}$ multilayer structure. No interface layers and no roughness contribution were considered. Although, as mentioned, the $C_{\nu l}^{\mu' \mu}$ functions may describe a variety of domain correlations, simulations were performed for the case of strongly-coupled layer antiferromagnet in remanence. By layer antiferromagnet we mean even number of magnetic layers of identical thickness resulting in zero net magnetization of the ML stack in remanence. Except for the trivial case of full in-plane saturation, the magnetic layers in an AF multilayer stack are broken into domains of different orientations. In remanence, we assume 180° domain walls of negligible thickness, i.e. the sublayer magnetizations also vanish (for further details see below). Strong coupling implies a strict plane-perpendicular domain correlation throughout the ML stack, a structure, in which the top layer unequivocally identifies the domain structure in the lower ones (say '+' and '-' type domains). The actual functional form of such AF domain correlation is given in the next section.

For the SMR simulations, the scattering geometry was selected so that the layer magnetizations lay both in the plane of the film and of scattering, i.e. parallel/antiparallel to the in-plane component of the wave vector, \mathbf{k}_{\parallel} , a condition for the appearance of the SMR specular AF reflection.¹⁶ All SMR curves and maps were calculated for the 14.4-keV Mössbauer resonance of ${}^{57}\text{Fe}$ ($\lambda = 0.086\text{ nm}$) for hyperfine magnetic fields of $\pm 33.08\text{ T}$ for the '+' and '-' type domains, respectively. The isomer shift and quadrupole splitting were set to zero (parameters for *bcc* iron at room temperature). The electronic susceptibilities for the $\lambda = 0.086\text{ nm}$ x-rays were taken from the Berkeley web site⁴⁷ for the various elements. The synchrotron bunch time t_{bunch} , and integration boundaries t_1 and t_2 were chosen according to the actual experimental values (see below).

For PNR simulations, monochromatic neutrons of wavelength $\lambda = 0.4\text{ nm}$ were assumed and the layer magnetizations were set parallel/antiparallel to the neutron spin and per-

pendicular to \mathbf{k}_{\parallel} . The nuclear scattering lengths used for Cr, ^{57}Fe and MgO are 3.6, 2.3, and 11.2 fm, respectively.⁴⁸ The magnetic scattering length $b_m(z) = C\mu(z)$, where $C = r_0\gamma/2 = 2.69542 \text{ fm}/\mu_B$, where r_0 is the classical electron radius, $\gamma = 1.91304$ is the magnetic moment of neutron in nuclear magnetons, $\mu(z)$ is the average magnetic moment per atom per unit volume at depth z , μ_B is the Bohr magneton. Numerically, $b_m(z)$ was set to ± 5.93 fm for the '+' and '-' type domains within the ^{57}Fe layers and zero otherwise.

The theory presented above was implemented in, and specular and off-specular intensity curves and maps (both SMR and PNR) were simulated by the data evaluation computer program EFFI (**E**nvironment **F**or **F**itting), which is freely downloadable.^{49,50}

A. Consequences of the finite coherence length

In the case of a 1:1 surface coverage of the '+' and '-' type domains, laterally averaging the magnetizations within a layer — as mentioned in the introduction — leads to a loss of the AF contrast and no AF Bragg peak in the specular reflectivity appears. However, when the lateral size of the domains is bigger than or comparable to the lateral coherence length¹⁹ of the applied radiation, a net layer magnetization is sampled within the coherence area and such intensity contributions are to be added incoherently.^{19,52,53} Consequently, a magnetic contrast appears in the specular reflectivity. In order to account for the effects of the finite coherence volume,¹⁸ the domain size is to be related to the lateral coherence area, the projection of the coherence volume¹⁸ to the top magnetic layer. (The lateral coherence length was reported to be 0.1 to 30 μm for neutrons⁵¹ and similar values can be derived for nuclear resonant photons.⁵²)

In order to account for the effects of the finite coherence volume,¹⁸ the domain size is to be related to the coherence area. In order to account for the effect of the finite coherence length we redefine the fractional area of a domain type, η_l^μ that was defined above for incident radiation with infinite coherence lengths. Indeed, as a first approximation, one can use Eq. (3.5) inside the coherence area within the top layer by exchanging A , the total area of the film, for the coherence area and relating the surface of type μ domains to the coherence area. In case of an antiferromagnet the domain type index μ identifies the '+' and '-' type domains ($\mu = +, -$). Using Eq. (3.6) one can introduce a specific magnetic bias parameter

η for the layers of even and odd index by the definition

$$\eta = \eta_{2i+1}^+ = 1 - \eta_{2i+1}^- = \eta_{2i}^- = 1 - \eta_{2i}^+ \quad (4.1)$$

with i being an integer.

In Fig. 1 simulated specular SMR intensity curves are displayed for different values of η . As expected, the η -dependence is restricted to the θ_{in} ($= \theta_{\text{out}}$) regions of 1/2- and 3/2-order AF Bragg reflections. As explained, there are no AF peaks for $\eta = 0.5$ and the magnetic contrast increases with increasing dominance of either '+' or '-' type domains. Since the coherence area is smaller than the illuminated area and it may have an arbitrary position, which can be identified by η , the integration in Eq. (2.17) is performed as a function of η . The off-specular intensity in (2.18) is calculated as

$$I_{\text{off}} = \int_0^1 p(\eta) I_{\text{off}}(\eta) d\eta, \quad (4.2)$$

where $p(\eta)$ is the normalized probability density of having a (magnetic) domain bias of η . We note that the probability function $p(\eta)$ depends both on the lateral domain structure and on the measurement geometry (source and slit dimensions, etc.). For the sake of simplicity, we consider here the case when the probability density $p(\eta)$ sharply peaks near 0 and 1 since strong specular SMR AF Bragg peaks can indeed be observed experimentally. Since the NRS spectra of a magnetic layer with k -parallel or a k -antiparallel directions of the hyperfine field can not be distinguished, the SMR AF Bragg peak is of the same shape and intensity irrespective of whether the AF structure starts with a k -parallel or a k -antiparallel layer on the top of the stack.¹³ Therefore the curves in Fig. 1 are identical for domain bias η and $1 - \eta$.

The specular curves in Fig. 1 are typical for an AF multilayer. For the above model structure and wavelength corresponding to the ⁵⁷Fe Mössbauer resonance energy the structural and AF Bragg peaks show up at $\theta_{\text{in}} = 11.3$ and $\theta_{\text{in}} = 6.7$ mrad, respectively. The Kiessig fringes,⁵⁵ characteristic of the total thickness of the ML, appear in all specular curves, however, due to the strong nuclear resonant absorption in the ⁵⁷Fe layers, their amplitude is strongly attenuated. Below the critical angle, the delayed reflected SMR intensity tends to zero at zero incident angle,^{56,57} whereas a non-resonant x-ray or PNR curve behaves 'normally' (i.e. tends to unity, corresponding to total reflection). This difference, as we shall see, leads to an augmented effect on the diffuse intensities.

B. Lateral correlation: domains

The domain structure within the top layer of the AF multilayer stack will be assumed laterally isotropic and statistically characterized by the correlation function of the top layer magnetization. For simplicity, we assume an exponential function and interpret the average domain size as the correlation length ξ of the exponential correlation function³⁰

$$\mathfrak{C}_{ll'}^{\mu\mu'}(\mathbf{r}_{\parallel}) = (-1)^{l+l'+1-\delta_{\mu\mu'}} \eta(1-\eta) \exp\left(-\frac{r_{\parallel}}{\xi}\right) \quad (4.3)$$

where δ is the Kronecker delta symbol. We assume the same correlation function for each values of indices observing an alternating sign corresponding to the strict plane-perpendicular AF correlation and an in-plane '+'/'-' domain model. The Fourier transform of Eq. (4.3) reads

$$C_{ll'}^{\mu\mu'}(\mathbf{K}_{\parallel}) = (-1)^{l+l'+1-\delta_{\mu\mu'}} \eta(1-\eta) \frac{2\pi\xi^2}{\left[1 + (K_{\parallel}\xi)^2\right]^{3/2}}, \quad (4.4)$$

which is then substituted into Eqs. (3.10) and (3.20) for calculating the off-specular PNR and SMR intensities, respectively.

C. Off-specular scattering: PNR and SMR

Figs. 2 and 3 show simulated ω -scans for the above model multilayer at $2\theta = 52$ mrad and $2\theta = 13.4$ mrad corresponding to the 1/2-order AF Bragg angle for different domain correlation lengths ξ using a single domain bias parameter $\eta = 0.1$, for PNR and SMR, respectively. Applying Eqs. (C6)-(C9) the kinematical approximation (first Born approximation, BA) is also shown. The curves were symmetrized by substituting the mirror image of $\omega < \theta$ in place of the $\omega > \theta$ region. The grounds of such substitution will be explained below. The BA curves display the same shape in the entire ξ -range and the off-specular scatter width is inversely proportional to ξ . The BA and symmetrized DIWA (called, henceforth, 'Symmetrized Distorted Incident-Wave Approximation', SDIWA) curves for PNR overlap almost in the entire angular range, the differences only develop near the critical incident and exit angles, i.e. at the Yoneda wings. For SMR, the SDIWA curves change their shape for different correlation lengths, since, as expected, the plane-perpendicular electronic and hyperfine depth profile, the energy- and polarization-dependent absorption embedded in the

Γ_l^μ functions have a strong influence on the shape of the off-specular scatter. Unlike in case of PNR, therefore, identifying the correlation length with the inverse width of the diffuse SMR scatter – without a proper evaluation of the entire reflectivity curve – can not be justified. Note, that the simulations were performed for the experimentally feasible neutron and nuclear photon wavelengths of $\lambda_n = 0.4$ nm and $\lambda_{^{57}\text{Fe}} = 0.086$ nm, respectively. Although the scattering amplitudes are comparable, the angular range between the Yoneda wings, consequently the angular width of validity of the BA approximation is considerably wider for the longer wavelength neutrons. This, however, does not effect the above statements on the qualitative differences between the PNR and SMR maps.

Figs. 4b and 5b display simulated two-dimensional ' $\theta_{\text{in}} - \theta_{\text{out}}$ ' maps for $\xi = 1$ μm correlation length with a single domain bias parameter $\eta = 0.1$ in the same DW approximation, corresponding to Eqs. 3.10 and 3.20 for PNR and SMR, respectively. The intensity is maximum along the diagonal specular line, and a broad diffuse intensity is observed around the half-order Bragg peaks. Similarly to the ω -scans, the $\theta_{\text{in}} < \theta_{\text{out}}$ semi-plane was mirrored onto the $\theta_{\text{in}} > \theta_{\text{out}}$ semi-plane. Only the diffuse I^{++} SDIWA and BA maps are displayed for PNR in Fig. 4. I^{+-} and I^{-+} maps are not shown since the spin-flip scattering vanishes due to the '+/'-' domains being assumed parallel/antiparallel with the incident neutron spin. Moreover, due to the small absorption of the neutrons, the ++ and -- maps (corresponding to the same layer structure with reversed layer sequence), are practically identical (and therefore not shown). It is not surprising that the Kiessig fringes are observed in both PNR and SMR diffuse scatter since the source for the diffuse intensity is the specular field. Due to the negligible absorption of the neutrons, the Kiessig contrast is stronger in PNR than in SMR. We may observe further symmetries in the PNR curve. As expected, the diffuse intensity around the structural Bragg node at $\theta_{\text{in}} = \theta_{\text{out}} = 52$ mrad is missing, since the diffuse scattering here is purely magnetic origin and the magnetic contributions cancel each other at the momentum transfer corresponding to the first order Bragg peak. Moreover, for $^{57}\text{Fe}/\text{Cr}$ for a 2:1 layer thickness ratio the 3/2-order Bragg reflection is forbidden, consequently, the node for the 2.62 nm(^{57}Fe)/1.28 nm(Cr) layer thickness ratio in Figs. 4, and 5 are very weak.

The ^{57}Fe $\theta_{\text{in}} - \theta_{\text{out}}$ SMR map in Fig. 5b shows a number of features different from that of PNR. Due to the dominance of energy-dependent absorption for resonant x-rays the SMR BA and SDIWA maps drastically differ. E.g., weak structural Bragg wings around

$\theta_{\text{in}} = \theta_{\text{out}} = 11.25$ mrad appears, but those fall below the typical experimental background level. Below the critical angle (unlike in cases of PNR or non-resonant x-rays), the *specular* SMR intensity, the source of the diffuse scatter, rapidly decreases to zero (*cf.* Fig. 1). Since, independently, due to the stronger absorption, the Kiessig fringes are suppressed in the SMR map in Fig. (5b), the intensity does not oscillate near Yoneda wings, which, as a result, appear broadened as compared to the PNR pattern in Fig. (4b). As a consequence, the total-reflection peak, being in the critical region, is somewhat difficult to distinguish from the 1/2–order AF Bragg node in Fig. (5b).

So far, by discussion of simulated SMR and PNR-scans and maps, we have shown, that the presented DIWA approach satisfactorily describes both the PNR and SMR off-specular intensity — except for *exit* angles below and around the critical angle of total reflection. In Appendix C the more exact DWBA SMR intensity formula is also given, which takes into account the distortions on both incident and emerging waves. However, the typical computation time needed for the DWBA calculation renders its usage completely impractical for fitting of diffuse synchrotron Mössbauer reflectograms even on advanced present-day computer architectures. Indeed, Eqs. (3.10) and (C6), differ only in the definition of Γ_l^u according to Eqs. (3.11) and (C7), for DIWA and for DWBA, respectively. Counting the number of the 2×2 complex matrix multiplications one can compare the speed of the two algorithms. On the one hand, in the DIWA equations (3.11) and (B7), one has to perform nine complex 2×2 matrix multiplications. On the other hand, in the DWBA Eq. (C7) $N_p \times 13$ complex 2×2 matrix multiplication have to be performed. N_p is typically ten. One may, therefore, conclude that DIWA, as derived here, is, at least, $10 \times 13/9 \approx 14$ times faster, than DWBA. Since, as previously explained, a single diffuse SMR map requires as much more computing time as the number of energy channels in the Mössbauer spectrum (typically 1024), this further factor in computing time would make such calculations extremely tedious.⁵⁸ Therefore an alternative approach was followed here.

In case of PNR, as a consequence of the negligible absorption of neutrons (Hermitian scattering potential), reciprocity is fulfilled. Conversely, the resonant Mössbauer medium is absorptive and gyrotropic and reciprocity can not be proved to hold in general.^{46,59} In fact, the violation of reciprocity in scattering on absorptive and gyrotropic media is still the subject of both experimental^{61,63,64} and theoretical^{46,62} works.⁶⁰

Nevertheless, for the special case under discussion, when all hyperfine magnetic fields are

aligned parallel/antiparallel to the wave vector, one may verify that reciprocity exactly holds. Indeed, in this case, the scattering amplitude is diagonal on the circular polarization basis throughout the whole multilayer and, therefore, Eq. (2.1) becomes uncoupled. Consequently the conventional proof of reciprocity to both eigenmodes is straightforward^{44,45} and the ' $\theta_{\text{in}} - \theta_{\text{out}}$ ' SMR maps become symmetrical. In view of the above, we prescribe reciprocity for both PNR and SMR and mirror the $\theta_{\text{in}} < \theta_{\text{out}}$ semi-plane onto the $\theta_{\text{in}} > \theta_{\text{out}}$ semi-plane. By doing so, the DWBA accuracy of the $\theta_{\text{in}} < \theta_{\text{out}}$ semi-plane is achieved by the present (faster) DIWA algorithm on the entire ' $\theta_{\text{in}} - \theta_{\text{out}}$ ' plane (with a further decrease of computing time by a factor of two. This symmetrizing procedure (SDIWA) was used to simulate the DIWA curves and maps in this paper (cf. Figs. 2, 3, 4, 5 and 6).

D. Experimental results and discussion

Two-dimensional experimental and simulated ' $\omega - 2\theta$ ' SMR maps of a [⁵⁷Fe/Cr] antiferromagnetic multilayer are presented in Fig. 6 in the vicinity of the antiferromagnetic (1/2-order) Bragg reflection (region marked by dashed lines in Fig. (5)). The MgO(001)/[⁵⁷Fe/Cr]₂₀ ML was prepared by molecular beam epitaxy at the IMBL facility of IKS Leuven, Belgium. Preparation and characterization of the sample has been described elsewhere.^{20,65,67} The layering was verified epitaxial and periodic, with thicknesses of 2.6 nm and 1.3 nm for the ⁵⁷Fe and Cr layers, respectively. SQUID magnetometry showed a saturation field of 0.9 T and AF coupling between neighboring Fe layers. According to previous studies on this multilayer,^{20,65,67} the Fe magnetizations at remanence align along the (100) and (010) perpendicular easy directions corresponding to the respective (110) and ($\bar{1}10$) directions of the MgO substrate. Experimental realization of alignment of domains along the k -vector was achieved in the following way. First a magnetic field of 1.6 T was applied perpendicular to k in one of the two equivalent in-plane directions of easy magnetization of the MgO(001)/[⁵⁷Fe/Cr]₂₀ ML, then the field was relaxed to remanence. By this procedure, due to the antiferromagnetic coupling between the layers, the sublayer magnetizations became aligned in the perpendicular easy direction, the two types of AF domains being only different in the top-layer magnetization direction.^{20,65,66}

Experimental $\omega - 2\theta$ SMR maps were recorded at the BL09XU nuclear resonance beam line⁶⁸ of SPring-8, Japan, using the 14.4 keV Mössbauer transition of ⁵⁷Fe by performing

sequential ω -scans in a 2θ -range. The synchrotron was operated in the 203-bunch mode, corresponding to a bunch separation time of $t_{\text{bunch}} = 23.6$ ns. The SR was monochromatized by a Si(4 2 2)/Si(12 2 2) double channel-cut high-resolution monochromator with a resolution of 6 meV. The specimen was mounted in grazing-incidence geometry with a sample-to-detector distance of 46 cm and receiving slit width of 0.1 mm. The delayed radiation was detected using three Hamamatsu avalanche photo diodes (APD) behind one another in order to increase detecting efficiency. The delayed photons were time integrated using the time windows given by $t_1 = 1.97$ ns and $t_2 = 21.63$ ns. For these special APDs the dead time was as small as below t_1 . Fig. 6 shows the two-dimensional experimental (a) and simulated (b) ' $\omega - 2\theta$ ' SMR maps in the vicinity of the 1/2-order Bragg position. In order to avoid transformation of the angles varied in the experiment, instead of the $\theta_{\text{in}} - \theta_{\text{out}}$ plane, data and simulations are displayed in the $\omega - 2\theta$ plane. Along the diagonal, the specular line was added taking the experimental receiving slit width into account. By trial and error and visual comparison, the best correlation function (4.4) was found with the correlation length of $\xi = 1.0$ μm . The simulation is in rather good agreement with the experimental data. A detailed discussion of experimental diffuse SMR scans including external field and field-history dependence of the domain structure will be reported elsewhere.

V. SUMMARY

In summary, expressions for the diffuse scattering intensity of grazing-incidence nuclear resonant scattering of synchrotron as well as polarized neutron radiation have been derived in a distorted-wave approximation. Distortion only of the incident wave was taken into account. In a common optical formalism,²¹ grazing-incidence (specular) x-ray, polarized neutron, nuclear resonance reflection, and grazing-incidence diffuse scattered intensity were calculated in terms of (geometrical) domain correlation functions and the specular field depth profile. The formula describes scattering by domains of rather general types with intra- and inter-plane correlations and is not restricted to the treatment of random lateral roughness. It was shown that, since the off-specular scatter shape is strongly dependent on the in-plane correlation length of a single exponential correlation function, without properly accounting for the specular field depth profile, no conclusions can be drawn on the shape of the domain correlation function. By prescribing the reciprocity (mirror symmetry of

the $\theta_{\text{in}} - \theta_{\text{out}}$ maps) the inadequacy of DIWA for critical exit angles was eliminated. In addition, reciprocity was shown to exactly hold for the most widely used case of SMR, i.e., when the layer magnetizations are parallel/antiparallel to the photon wave vector. The code based on the presented theory is suitable for simulation of diffuse SMR maps in a feasible calculation time, which is not yet the case for the DWBA formulae presented in Appendix C. Off-specular SMR and PNR ω -scans and $\theta_{\text{in}} - \theta_{\text{out}}$ maps of an antiferromagnetic [Fe/Cr] multilayer were calculated and compared to each other in order to show the different features of diffuse scattering of nuclear resonant synchrotron radiation and polarized neutrons. As an application of the presented theory, $\omega - 2\theta$ nuclear resonant diffuse scattering maps of an $\text{MgO}/[{}^{57}\text{Fe}(2.62\text{ nm})/\text{Cr}(1.28\text{ nm})]_{20}$ multilayer were simulated and, using an exponential in-plane correlation function, a layer magnetization correlation length of $\xi = 1.0\ \mu\text{m}$ was derived for the ML demagnetized from easy axis saturation to remanence.

APPENDIX A: GENERAL SOLUTION OF THE COHERENT FIELD EQUATION

The solution of Eq. (2.3) was given in Refs.^{21,27,49} where, using the derivative field $\Phi_{\text{coh}}(r_{\perp}) = (ik \sin \theta)^{-1} \Psi'_{\text{coh}}(r_{\perp})$, the second-order differential equation regarding to $\Psi_{\text{coh}}(\mathbf{r})$, was replaced by a set of first-order differential equations,²¹ providing the solution

$$\begin{pmatrix} \Phi(k_{\perp}, r_{\perp}) \\ \Psi(k_{\perp}, r_{\perp}) \end{pmatrix} = L(k_{\perp}, r_{\perp}) \begin{pmatrix} \Phi(k_{\perp}, 0) \\ \Psi(k_{\perp}, 0) \end{pmatrix}, \quad (\text{A1})$$

where L is the 4×4 characteristic matrix of the system,^{21,27,49} $k_{\perp} = k \sin \theta$ is the plane-perpendicular component of the wave number vector of the incident plane wave, which latter dependence we drop in this appendix. Here Ψ and Φ are coherent fields; the notation 'coh' has been dropped. The physical meaning of Eq. (A1) is that there exists a linear connection expressed by the characteristic matrix L between the fields at depth $r_{\perp} = 0$ and at an arbitrary depth r_{\perp} . Taking into account the boundary conditions, the field at the top surfaces of the system ($r_{\perp} = 0$) is

$$\Psi(0) = \Psi^{\text{in}} + R_{\text{sp}} \Psi^{\text{in}}, \quad (\text{A2})$$

i.e., the sum of the incident Ψ^{in} and the reflected $R_{\text{sp}} \Psi^{\text{in}}$ waves so that Eq. (A1) reads

$$\begin{pmatrix} \Phi(r_{\perp}) \\ \Psi(r_{\perp}) \end{pmatrix} = L(r_{\perp}) \begin{pmatrix} \Psi^{\text{in}} - R_{\text{sp}} \Psi^{\text{in}} \\ \Psi^{\text{in}} + R_{\text{sp}} \Psi^{\text{in}} \end{pmatrix} \quad (\text{A3})$$

where the concept of impedance tensors by Ref.⁶⁹ was used, taking into account that the fields at $r_{\perp} = 0$ are in vacuum (see Eqs. (21) and (22) of Ref.²¹). Expressing the second component from Eq. (A3), the field at an arbitrary depth r_{\perp} we have

$$\Psi(r_{\perp}) = [L^{[21]}(r_{\perp})(I - R_{\text{sp}}) + L^{[22]}(r_{\perp})(I + R_{\text{sp}})] \Psi^{\text{in}} \quad (\text{A4})$$

and using the notation $T(r_{\perp}) = L^{[21]}(r_{\perp})(I - R_{\text{sp}}) + L^{[22]}(r_{\perp})(I + R_{\text{sp}})$ the solution of the three-dimensional homogeneous wave equation is

$$\Psi_{\text{coh}}(\mathbf{k}, \mathbf{r}) = T(k_{\perp}, r_{\perp}) \Psi^{\text{in}} \exp(i\mathbf{k}_{\parallel} \mathbf{r}_{\parallel}). \quad (\text{A5})$$

APPENDIX B: CALCULATION OF THE $T_l(k_{\perp}, k'_{\perp})$ FOURIER INTEGRALS

In this appendix the analytical calculation of the integral (2.12) is given. The 4×4 characteristic matrix^{27,69} of an arbitrary homogeneous multilayered film with layers $l = 1, \dots, S$ is

$$L = L_S \dots L_2 L_1 \quad (\text{B1})$$

where

$$L_l = \begin{pmatrix} \cosh(kd_l F_l) & \frac{1}{x} F_l \sinh(kd_l F_l) \\ x F_l^{-1} \sinh(kd_l F_l) & \cosh(kd_l F_l) \end{pmatrix} \quad (\text{B2})$$

is the characteristic matrix of the l^{th} homogeneous layer^{21,27} with d_l being the thickness of the l^{th} layer, $x = i \sin \theta$ and the 2×2 matrix $F_l = \sqrt{-I \sin^2 \theta - \chi_l}$. We note that L depends on $k_{\perp} = k \sin \theta$, which dependence is not indicated in this Appendix. At depth r_{\perp} measured from the top of the ML the position vector points into layer $j < S$. The vector r_{\perp} totally covers the first $j - 1$ layers therefore the characteristic matrix at depth r_{\perp} can be written as

$$L(r_{\perp}) = L_j(r_{\perp} - D_{j-1}) \cdot L_{(j-1)} \quad (\text{B3})$$

where $D_{j-1} = \sum_{l=1}^{j-1} d_l$ is the total thickness of layers up to layer $j - 1$ and $L_{(j-1)} = L_{j-1} \dots L_1$ is the characteristic matrix of layers $1, \dots, j - 1$. We note that layer j is only partially covered by the depth interval, which is indicated by the argument $(r_{\perp} - D_{j-1})$ in Eq. (B3) instead of the total thickness d_j . It is also important to note that $L(r_{\perp})$ depends on the thicknesses and susceptibilities of all covered layers and, furthermore, that it also depends on the angle of grazing incidence θ .

Using Eqs. (2.8), (B2) and (B3) the integral (2.12) can be analytically calculated. Indeed, the two integrals

$$I_j^+ = \frac{1}{\sqrt{2\pi}} \int_{Z_j} dr_{\perp} \exp(-ik'_{\perp} r_{\perp}) \sinh[k(r_{\perp} - D_{j-1}) F_j] \quad (\text{B4a})$$

$$I_j^- = \frac{1}{\sqrt{2\pi}} \int_{Z_j} dr_{\perp} \exp(-ik'_{\perp} r_{\perp}) \cosh[k(r_{\perp} - D_{j-1}) F_j] \quad (\text{B4b})$$

result in

$$I_j^+ = \alpha_j + \beta_j \quad (\text{B5a})$$

$$I_j^- = \alpha_j - \beta_j, \quad (\text{B5b})$$

with

$$\alpha_j = \exp(-ik'_{\perp} D_{j-1}) \left[(K_j^-)^{-1} \exp\left(\frac{d_j}{2} K_j^-\right) \sinh\left(\frac{d_j}{2} K_j^-\right) \right] \quad (\text{B6a})$$

$$\beta_j = \exp(-ik'_{\perp} D_{j-1}) \left[(K_j^+)^{-1} \exp\left(-\frac{d_j}{2} K_j^+\right) \sinh\left(\frac{d_j}{2} K_j^+\right) \right]. \quad (\text{B6b})$$

Here $K_j^{\pm} = kF_j \pm ik'_{\perp} I$. Finally the required expression has the form

$$T_l(k_{\perp}, k'_{\perp}) = \left[xF_j^{-1} I_j^+ L_{(j-1)}^{[11]} + I_j^- L_{(j-1)}^{[21]} \right] (I - R_{\text{sp}}) + \left[xF_j^{-1} I_j^+ L_{(j-1)}^{[12]} + I_j^- L_{(j-1)}^{[22]} \right] (I + R_{\text{sp}}). \quad (\text{B7})$$

Eq. (B7) is physically the Fourier transform of the depth-profile function of the coherent field and we emphasize again its dependence on k_{\perp} .

APPENDIX C: DWBA OFF-SPECULAR INTENSITY FORMULAE

As it was noted in Sections II and III, the diffuse intensity expressions (2.18) and (3.10) differ from the result of DWBA. Indeed, the DWBA transition matrix element $\langle \beta | \mathbb{T} | \alpha \rangle$ of the transition between the eigenstates $|\alpha\rangle$ and $|\beta\rangle$ of the interaction-free Hamiltonian is

$$\langle \beta | \mathbb{T} | \alpha \rangle \approx (\kappa_{1\beta}^{T-}, V_2 \kappa_{1\alpha}^+), \quad (\text{C1})$$

where \mathbb{T} is the transition matrix, V_2 is the perturbing potential, $\kappa_{1\alpha}^+$ and $\kappa_{1\beta}^{T-}$ are the retarded and the advanced solutions of the unperturbed Hamiltonian and adjoint Hamiltonian,

asymptotically related to $|\alpha\rangle$ and $|\beta\rangle$, respectively.⁴⁴ The interaction potential $V = k^2\chi$ is split according to Eq. (2.4) to a sum

$$V = V_1 + V_2 = k^2\bar{\chi} + k^2(\chi - \bar{\chi}), \quad (\text{C2})$$

where the wave equation is exactly soluble for $V_1 = k^2\bar{\chi}$ and $V_2 = k^2(\chi - \bar{\chi})$ is regarded as the perturbing potential. The arguments of χ and $\bar{\chi}$ were dropped for the sake of simplicity. According to the concept used in this paper, the initial and final states $|\alpha\rangle$ and $|\beta\rangle$ are plane waves with wave vectors \mathbf{k} and \mathbf{k}' , respectively.

The solution of the unperturbed equation (2.3), having only the V_1 potential, was given in Eq. (2.7). One notes that Eq. (2.7) is the retarded solution of Eq. (2.3), therefore

$$\kappa_{1\alpha}^+ = T(k_\perp, r_\perp) \Psi^{\text{in}} \exp(i\mathbf{k}_\parallel \mathbf{r}_\parallel). \quad (\text{C3})$$

The advanced solution can be given similarly, taking into account that the advanced solution is related to the emerging plane wave rather than to the incoming wave considered in Eq. (A2). Therefore using

$$\Psi(0) = R_{\text{sp}}^{-1} \Psi^{\text{out}} + \Psi^{\text{out}} \quad (\text{C4})$$

and V_1^\dagger instead of V_1 , the advanced solution can be written as

$$\kappa_{1\beta}^{T-} = \widehat{T}(-k'_\perp, r_\perp) \Psi^{\text{out}} \exp(i\mathbf{k}'_\parallel \mathbf{r}_\parallel), \quad (\text{C5})$$

where \widehat{T} means that in Eq. (A5) the specular reflectivities are inverted and the adjoint susceptibilities are used. Applying Eqs. (C1), (C3), (C5), (3.3), (3.4), (3.8) and (3.12) the diffuse intensity is

$$I_{\text{off}}(E) = k^4 \sum_{l'l''} C_{l'l''}^{\mu'\mu}(\mathbf{K}_\parallel) \text{Tr} \left[\Gamma_{l''}^{\mu'}(E)^\dagger \Gamma_l^\mu(E) \rho \right] \quad (\text{C6})$$

similarly to Eq. (3.10), however, the definition of Γ_l^μ being

$$\Gamma_l^\mu(k_\perp, k'_\perp, E) = \int_{Z_l} dr_\perp \widehat{T}(-k'_\perp, r_\perp)^\dagger \chi_l^\mu(E) T(k_\perp, r_\perp). \quad (\text{C7})$$

different from that given in Eq. (3.11). The integral (C7) can be analytically calculated following the method presented in Appendix B. Comparing Eq. (C7) with Eqs. (2.12) and (3.11) one can realize that the present result of Eq. (3.10) can be also obtained from the DWBA by taking

$$\widehat{T}(-k'_\perp, r_\perp)^\dagger \approx I \exp(-ik'_\perp r_\perp), \quad (\text{C8})$$

which is valid only for exit angles (θ') above the critical angle. This statement is consistent with ignoring the scattering of the diffuse field as assumed in section II. We also note that approximation

$$T(k_{\perp}, r_{\perp}) \approx I \exp(ik_{\perp}r_{\perp}) \quad (\text{C9})$$

together with (C8) are identical to the conventional 1st order Born approximation.

ACKNOWLEDGMENTS

This work was partly supported by the Hungarian Scientific Research Fund (OTKA) and National Office for Research and Technology of Hungary under Contract numbers T047094 and NAP-Veneus'05 as well as by the European Community under the Specific Targeted Research Project Contract No. NMP4-CT-2003-001516 (DYNASYNC). The authors gratefully acknowledge the beam time supplied free of charge by the Japan Synchrotron Radiation Institute (JASRI) for experiment No: 2002B239-ND3-np. Our gratitude goes to *A.Q. Baron* (SPring-8, JASRI) for his kind supply of the fast Hamamatsu APD detectors, *J. Dekoster* (IKS Leuven) for preparing the multilayer sample and to *D. G. Merkel* (KFKI RMKI Budapest) for his assistance in data processing. One of the authors (LD) gratefully acknowledges the financial support by the Deutscher Akademischer Austauschdienst (DAAD).

* Electronic address: deak@rmki.kfki.hu

¹ K. N. Stoev, K. Sakurai, *Spectrochimica Acta*, Part B 54 (1999) 41.

² M. Lax, *Rev. Mod. Phys.* 23 (1951) 287.

³ X.-L. Zhou, S.-H. Chen, *Phys. Rep.* 257 (1995) 223.

⁴ J. Daillant, A. Gibaud (eds.) "X-Ray and Neutron Reflectivity: Principles and Applications" *Lecture Notes in Physics* m 58. Springer-Verlag, New York, 1999.

⁵ G.P. Felcher, *Physica B* 192 (1993) 137.

⁶ C.F. Majkrzak, *Physica B* 173 (1991) 75.

⁷ S.K. Sinha, *Physica B* 173 (1991) 25.

⁸ J.P. Hannon, G.T. Trammell, M. Blume, and Doon Gibbs, *Phys. Rev. Lett.* 61 (1988) 1245.

- ⁹ D.B. Mac Whan, *J. Synchrotron Radiat.* 1 (1994) 83., and references therein.
- ¹⁰ T.P.A. Hase, I. Pape, B.K. Tanner, H. Dürr, E. Dudzik, G. van der Laan, C.H. Marrows and B.J. Hickey, *Phys. Rev. B* 61 (2000) R3792.
- ¹¹ V. Lauter-Pasyuk, H.J. Lauter, B. Toperverg, O. Nikonov, E. Kravtsov, M.A. Milyaev, L. Romashev and V. Ustinov, *Physica B* 283 (2000) 194.
- ¹² S. Langridge, J. Schmalian, C.H. Marrows, D.T. Dekadjevi and B.J. Hickey, *Phys. Rev. Lett.* 85 (2000) 4964.
- ¹³ D.L. Nagy, L. Bottyán, L. Deák, E. Szilágyi, H. Spiering, J. Dekoster and G. Langouche, *Hyp. Int.* 126 (2000) 353.
- ¹⁴ L. Deák, L. Bottyán, M. Major, D.L. Nagy, H. Spiering, E. Szilágyi and F. Tanczikó, *Hyp. Int.* 144/145 (2002) 45.
- ¹⁵ T.S. Toellner, W. Sturhahn, R. Röhlberger, E.E. Alp, C.H. Sowers and E.E. Fullerton, *Phys. Rev. Lett.* 74 (1995) 3475.
- ¹⁶ A.I. Chumakov, L. Niesen, D.L. Nagy and E.E. Alp, *Hyp. Int.* 123/124 (1999) 427.B.
- ¹⁷ R. Röhlberger, J. Bansmann, V. Senz, K.L. Jonas, A. Bettac, K.H. Meiwes-Broer, O. Leupold, *Phys. Rev. B.* 67 (2003) 245412.
- ¹⁸ L. Mandel and E. Wolf, "Optical coherence and quantum optics" p 155, (Cambridge University Press, 1995)
- ¹⁹ B.T. Toperverg, *Physica B* 297 (2001) 160.
- ²⁰ D.L. Nagy, L. Bottyán, B. Croonenborghs, L. Deák, B. Degroote, J. Dekoster, H.J. Lauter, V. Lauter-Pasyuk, O. Leupold, M. Major, J. Meersschaut, O. Nikonov, A. Petrenko, R. Ruffer, H. Spiering and E. Szilágyi, *Phys. Rev. Lett.* 88 (2002) 157202.
- ²¹ L. Deák, L. Bottyán, D.L. Nagy, and H. Spiering, *Physica B* 297 (2001) 113.
- ²² A.M. Afanas'ev and Yu. Kagan, *Sov. Phys. —JETP* 21 (1965) 215.
- ²³ J.P. Hannon and G.T. Trammell, *Phys. Rev.* 186 (1969) 306.
- ²⁴ J.P. Hannon, G.T. Trammell, M. Mueller, E. Gerdau, R. Ruffer, and H. Winkler, *Phys. Rev. B* 32 (1985) 6363.
- ²⁵ S.M. Irkaev, M.A. Andreeva, V.G. Semenov, G.N. Belozerskii and O.V. Grishin, *Nucl. Instrum. Methods B* 74 (1993) 545.
- ²⁶ S.M. Irkaev, M.A. Andreeva, V.G. Semenov, G.N. Belozerskii, and O.V. Grishin, *Nucl. Instrum. Methods B* 74 (1993) 554.

- ²⁷ L. Deák, L. Bottyán, D.L. Nagy and H. Spiering, Phys. Rev. B. 53 (1996) 6158.
- ²⁸ R. Röhlberger, Hyp. Int. 123/124 (1999) 301.
- ²⁹ R. Röhlberger, Hyp. Int. 123/124 (1999) 455.
- ³⁰ S.K. Sinha, E.B. Sirota, S. Garoff, H.B. Stanley, Phys. Rev B 38 (1988) 2297.
- ³¹ B.T. Toperverg, O. Nikonov, V. Lauter-Pasyuk, H.J. Lauter, Physica B 297 (2001) 169.
- ³² V. Lauter-Pasyuk et al., J. Magn. Magn. Mater. 226-230 (2001) 1694.
- ³³ A. Rühm, B.P. Toperverg, H. Dosch, Phys. Rev. B. 60 (1999) 16073.
- ³⁴ G. H. Vineyard, Phys. Rev. B. 26 (1982) 4146.
- ³⁵ H. Dosch, "Critical Phenomena at Surfaces and Interfaces" (Springer-Verlag, New York 1992).
- ³⁶ G.Ljungdahl and S.W.Lovesey, Physica Scripta 53 (1996) 734.
- ³⁷ G.P. Felcher, R.O. Hilleke, R.K. Crawford, J. Haumann, R. Kleb, and G. Ostrowski, Rev. Sci. Instrum 58 (1987) 609.
- ³⁸ L.G. Parratt, Phys. Rev. 95 (1954) 359.
- ³⁹ C.F. Majkrzak, Physica B 156&157 (1989) 619.
- ⁴⁰ B. Nickel, A. Rühm, W. Donner, J. Major, H. Dosch, A. Schreyer, H. Zabel, and H. Hublot, Rev. Sci. Instrum 72 (2001) 163.
- ⁴¹ J.P. Hannon, N.V. Hung, G.T. Trammell, E. Gerdau, M. Mueller, R. Rüffer, and H. Winkler, Phys. Rev. B 32 (1985) 5068.
- ⁴² M. Blume and O.C. Kistner, Phys. Rev. 171 (1968) 417.
- ⁴³ G.T Trammell and J.P. Hannon, Phys. Rev B 18 (1978) 165.
- ⁴⁴ Leonard I. Schiff, "Quantum mechanics" p 327 (McGraw-Hill, 1955).
- ⁴⁵ M. Born and E. Wolf, "Principles of optics", (Cambridge University Press, 7th edition, 1999)
- ⁴⁶ R.J. Potton, Rep. Prog. Phys **67** (2004) 717.
- ⁴⁷ L. Henke, Atomic data and nuclear data tables 54, 1993, 181; see also http://henke.lbl.gov/optical_constants/getdb2.html
- ⁴⁸ Neutron News, Vol. 3, No. 3, 1992, pp. 29-37, <http://www.ncnr.nist.gov/resources/n-lengths/>
- ⁴⁹ H. Spiering, L. Deák, and L. Bottyán, Hyp. Int. 125 (2000) 197.
- ⁵⁰ The computer program EFFI is available from <ftp://nucssp.rmki.kfki.hu/pub/effi>
- ⁵¹ A. Paul, E. Kentzinger, U. Rücker, D. E. Bürgler, and Thomas Brückel, Phys. Rev. B **73**, (2006) 94441.

- ⁵² A. Q. R. Baron, A. I. Chumakov, H. F. Grünsteudel, H. Grünsteudel, L. Niesen, and R. Rüffer, PRL 77 (1996) 4808.
- ⁵³ S.K. Sinha, M. Tolan, A. Gibaud, Phys. Rev. B **57** (1998) 2740.
- ⁵⁴ S. W. Lovesey, "Theory of Neutron Scattering from Condensed Matter Volume II: Polarization Effects and Magnetic Scattering" Clarendon Press, 1986.
- ⁵⁵ H. Kiessig, Annalen der Physik (1931) 769.
- ⁵⁶ L. Deák, L. Bottyán, D.L. Nagy, Hyp. Int. 92 (1994) 1083.
- ⁵⁷ A.Q.R. Baron, J. Arthur, S.L. Ruby, A.I. Chumakov, G.V. Smirnov, G.S. Brown, Phys. Rev. B **50**, (1994) 10354.
- ⁵⁸ The calculation time for the diffuse SMR map 100×100 points in Fig. 5 on a 64-bit PC with 1024 Mb RAM and AMD Athlon 3000+ processor running a single user process under SuSe Linux 10.0 was 12 hours. The estimated DWBA calculation time is exactly one week.
- ⁵⁹ A.H. Huffman, Phys. Rev. D **1**, (1970) 890.
- ⁶⁰ The proof of the corresponding reciprocity *theorem* is a subject of a number of theoretical work.^{44,45,46,70,71,72} Rigorous proof was given for the cases of real^{44,70} (like in PNR) and for complex and short range, polarization-independent^{44,45,72} scattering potentials.⁵⁹ Whether or not reciprocity actually holds for the case of nuclear resonant photons, where the susceptibility and, consequently, $k^2\chi$, the scattering potential is complex and polarization dependent, is beyond the scope of the present discussion.
- ⁶¹ V.A. Chernov, V.I. Kondratiev, N.V. Kovalenko, S.V. Mytnichenko, K.V. Zolotarev, Physica B **357**, (2005) 232.
- ⁶² S.V. Mytnichenko, Physica B **355**, (2005) 244.
- ⁶³ V.A. Chernov, E.D. Chkhalo, N.V. Kovalenko, S.V. Mytnichenko, Nuclear Instruments and Methods in Physics Research A **448**, (2000) 276.
- ⁶⁴ V.A. Chernov, N.V. Kovalenko, S.V. Mytnichenko and A.I. Toropov, Act. Crist. A 59, (2003) 551.
- ⁶⁵ L. Bottyán, L. Deák, J. Dekoster, E. Kunnen, G. Langouche, J. Meersschaut, M. Major, D.L. Nagy, H.D. Rüter, E. Szilágyi, K. Temst, J. Magn. Magn. Mater. **240**, (2002) 514.
- ⁶⁶ D.L. Nagy, L. Bottyán, L. Deák, B. Degroote, O. Leupold, M. Major, J. Meersschaut, R. Rüffer, E. Szilágyi, J. Swerts, K. Temst, Phys. Stat. Sol. (a) 189 (2002) 591.
- ⁶⁷ F. Tanczikó, L. Deák, D.L. Nagy, L. Bottyán, Nucl. Instr. Meth. Phys. Res. B **226**, (2004) 461.

- ⁶⁸ Y. Yoda, M. Yabashi, K. Izumi, X.W. Zhang, S. Kishimoto, S. Kitao, M. Seto, T. Mitsui, T. Harami, Y. Imai, and S. Kikuta, Nucl. Instrum. Methods Phys. Res. A **467**, (2001) 715.
- ⁶⁹ G.M. Borzdov, L.M. Barskovskii, and V.I. Lavrukovich, Zh. Prikl. Spektrosk. 25 (1976) 526.
- ⁷⁰ David S. Saxon, Phys. Rev. **100** (1955) 1771.
- ⁷¹ P. Hillion, J. Optics **9** (1978) 173.
- ⁷² R. Carminati, J.J. Sáenz, J.-J. Greffet, and M. Nieto-Vesperinas, Phys. Rev. **A** 62 (2000) 012712

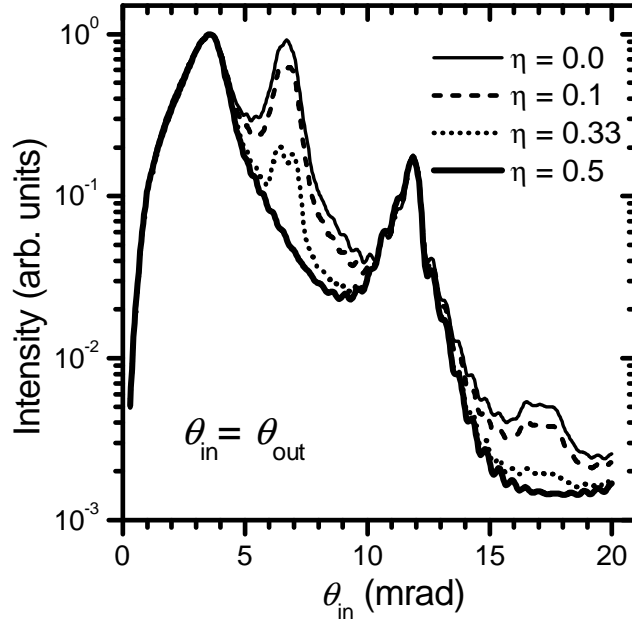


FIG. 1: Simulated ^{57}Fe specular synchrotron Mössbauer reflectograms ($\theta - 2\theta$ scans) of the $\text{MgO}/[^{57}\text{Fe}(2.62\text{ nm})/\text{Cr}(1.28\text{ nm})]_{20}$ antiferromagnetic multilayer with sublayer magnetizations parallel and antiparallel to the wave vector for different domain bias parameters, η indicated in the figure.

Fig. 1		L. Deák et al.
Perturbative Theory of Grazing Incidence Nuclear Resonance Diffuse Scattering of Synchrotron Radiation		

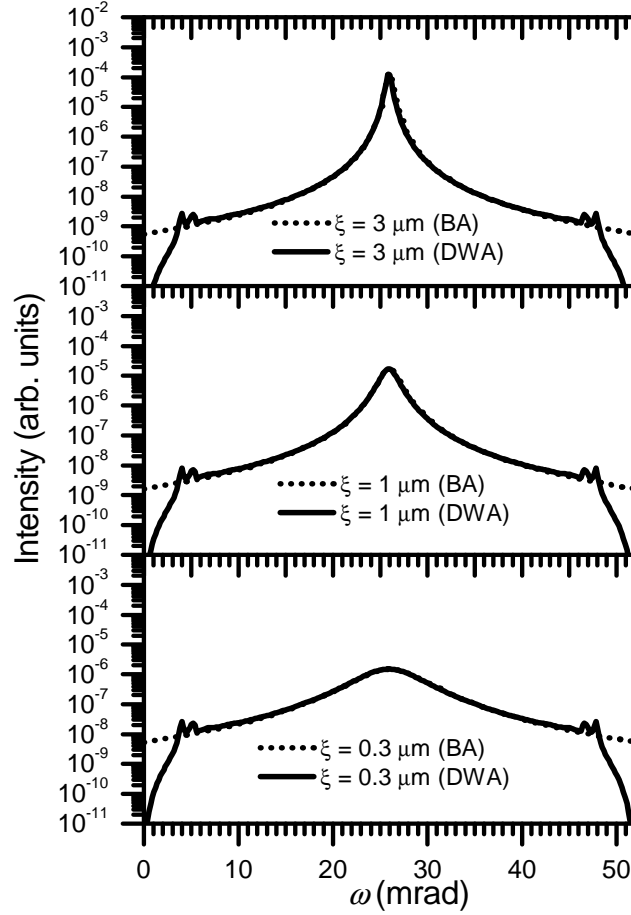


FIG. 2: Simulated off-specular PNR ω -scans (I^{++}) calculated for the MgO/ ^{57}Fe (2.62 nm)/Cr (1.28 nm) $_{20}$ antiferromagnetic multilayer with $\lambda = 0.4$ nm and detector position 2θ fixed at the 1/2-order antiferromagnetic Bragg peak position for various correlation lengths, ξ indicated in the figure. A single domain bias parameter of $\eta = 0.1$ was used. Dotted and solid lines show the BA and SDIWA simulations, respectively.

Fig. 2		L. Deák et al.
Perturbative Theory of Grazing Incidence Nuclear Resonance Diffuse Scattering of Synchrotron Radiation		

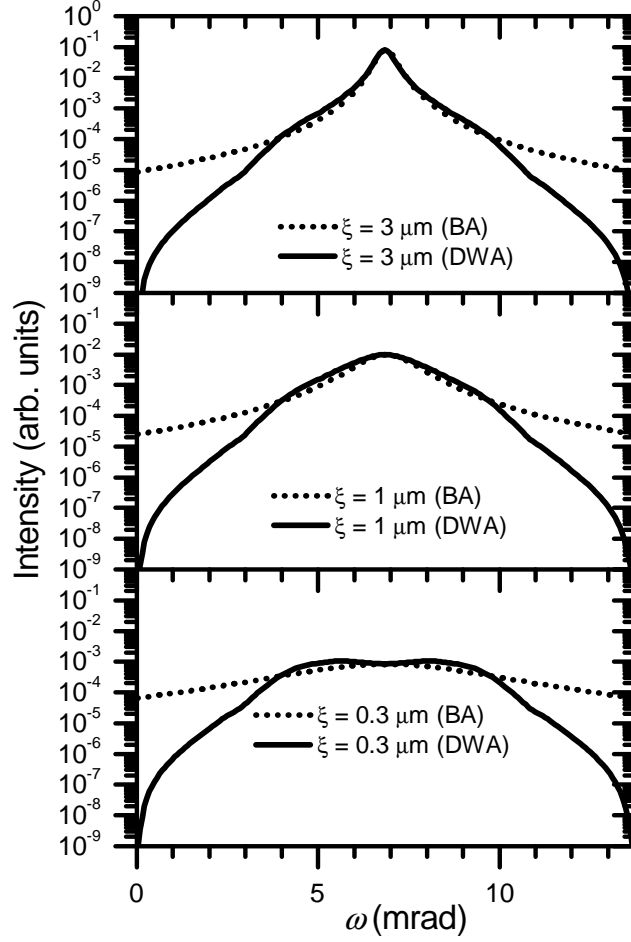


FIG. 3: Simulated off-specular SMR ω -scans calculated for the $\text{MgO}/[{}^{57}\text{Fe}(2.62\text{ nm})/\text{Cr}(1.28\text{ nm})]_{20}$ antiferromagnetic multilayer with $\lambda = 0.086\text{ nm}$ of the ${}^{57}\text{Fe}$ Mössbauer radiation and the detector position 2θ fixed at the 1/2-order antiferromagnetic Bragg peak position for various correlation lengths, ξ indicated in the figure. A single domain bias parameter of $\eta = 0.1$ was used. Dotted and solid lines show the BA and SDIWA simulations, respectively.

Fig. 3		L. Deák et al.
Perturbative Theory of Grazing Incidence Nuclear Resonance Diffuse Scattering of Synchrotron Radiation		

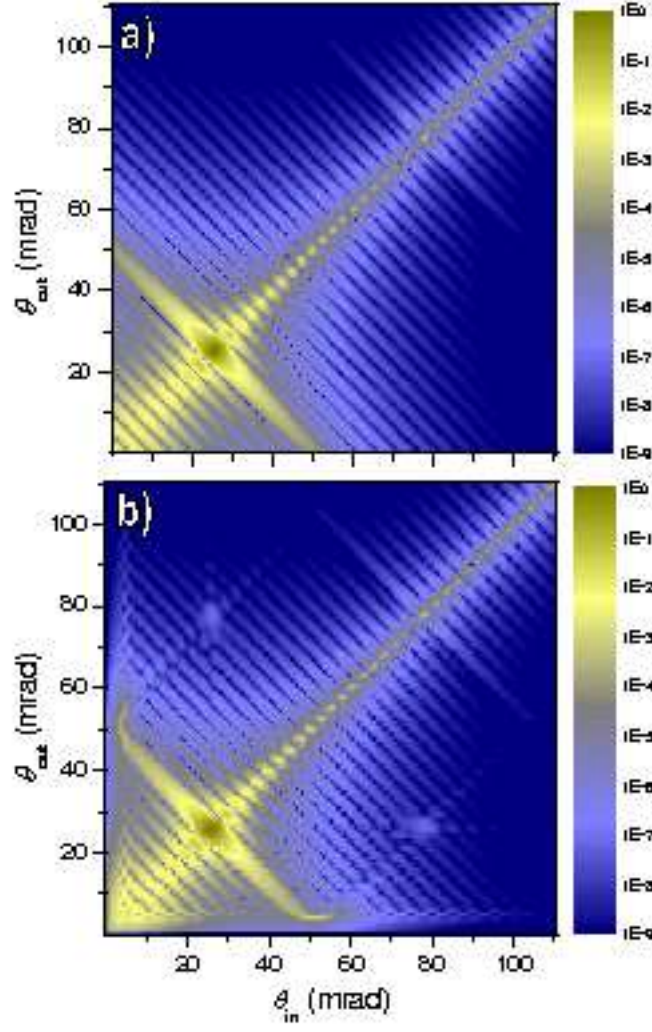


FIG. 4: Simulated ' $\theta_{\text{in}} - \theta_{\text{out}}$ ' PNR diffuse intensity maps for the MgO/ ^{57}Fe (2.62 nm)/Cr (1.28 nm) $_{20}$ antiferromagnetic multilayer structure. The intensities are normalized and shown on a logarithmic color scale. BA (a) and SDIWA (b) I^{++} intensities are shown. A single domain bias parameter of $\eta = 0.1$ was used.

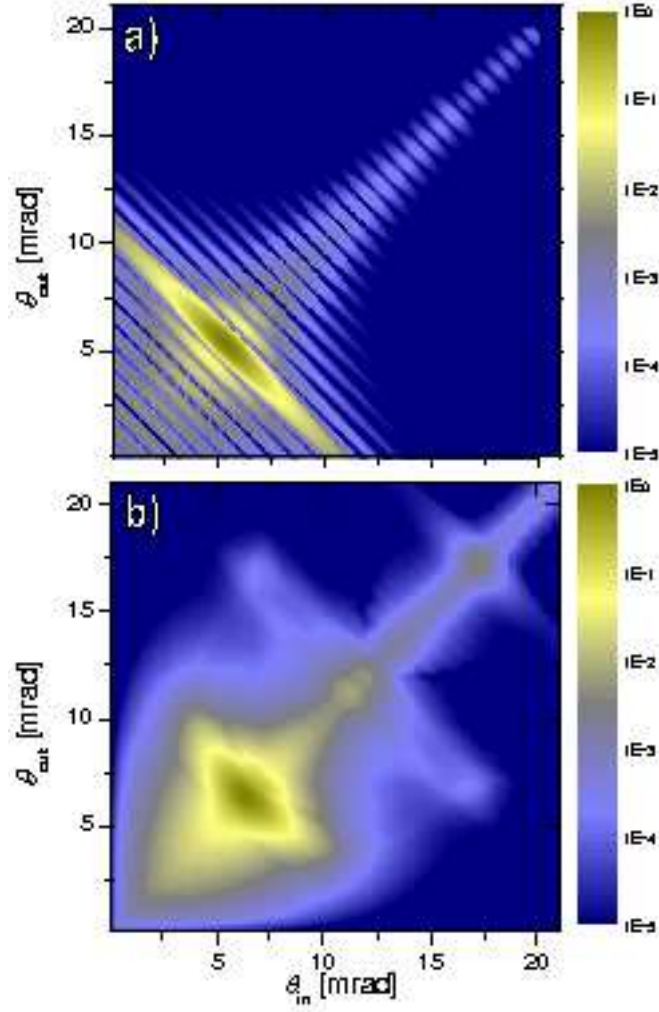


FIG. 5: Simulated ' $\theta_{\text{in}} - \theta_{\text{out}}$ ' SMR diffuse intensity maps of the $\text{MgO}/[{}^{57}\text{Fe}(2.62\text{ nm})/\text{Cr}(1.28\text{ nm})]_{20}$ antiferromagnetic multilayer structure around the 1/2-order antiferromagnetic Bragg peak using the BA (a) and the SDIWA (b). The intensities are shown on a logarithmic color scale and are normalized. A single domain bias parameter of $\eta = 0.1$ was used.

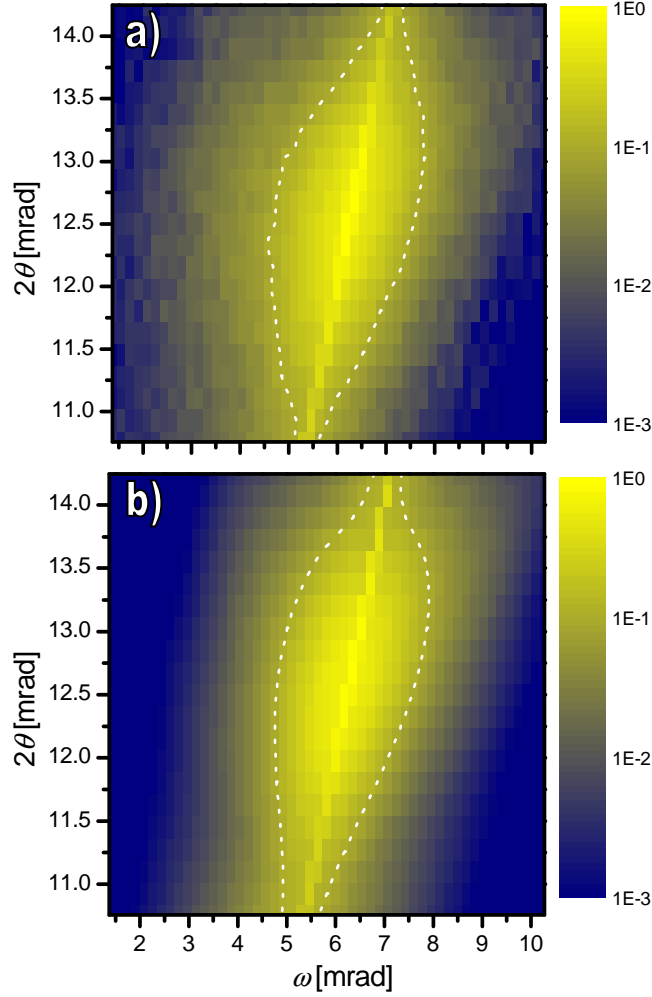


FIG. 6: Measured (a) and simulated (b) ' $\omega - 2\theta$ ' SMR diffuse intensity maps of the $\text{MgO}/[{}^{57}\text{Fe}(2.62\text{ nm})/\text{Cr}(1.28\text{ nm})]_{20}$ antiferromagnetic multilayer in the vicinity of the 1/2-order antiferromagnetic Bragg peak. The intensities are normalized and shown on a logarithmic color scale. Map (b) was simulated using Eqs. 3.20, 4.3 and 4.4 with $\xi = 1.0\ \mu\text{m}$ domain correlation length. The dotted white line shows the 10% level of the maximum intensity.

Fig. 6		L. Deák et al.
Perturbative Theory of Grazing Incidence Nuclear Resonance Diffuse Scattering of Synchrotron Radiation		